Chapter 1

Simple Experiments Under Isca Framework

1.1 Introduction

1.1.1 Isca model

Isca is an open-source framework for the idealized modeling of global circulation of atmospheres, which provides various options for users to setup experiments for their own interests [Vallis et al., 2018]. These options include dry and moist models, various convection and radiation schemes, a variety of land/sea configurations and different parameters for other planetary atmospheres. Taking the radiation scheme in Isca as an example, the choices include two gray radiation schemes (gray means that radiation in different wavelength is treated equally), which we call Frierson [Frierson et al., 2006] and Byrne & O'Gorman (BOG hereafter) [Byrne and O'Gorman, 2013]; an intermediate scheme with two infrared bands and one solar band, similar to Geen et al. [2016]; and a full radiation scheme, the multiband correlated-k Rapid Radiative Transfer Model (RRTM) [Clough et al., 2005]. In fact, the plentiful options in Isca offer users an opportunity to explore the models with different levels of complexity under the same experimental setup.

However, there are no interactive cloud schemes, dynamical ocean and sophisticated land-surface models in Isca currently, compared to the comprehensive climate

models. In general, clouds associated with weather and climate phenomena are the essential parts of climate system, but the simulations of clouds and their feedbacks have large uncertainties in current general circulation models (GCMs). For example, as pointed by Ceppi et al. [2017], cloud feedback is the largest source of intermodel spread in equilibrium climate sensitivity in the recent Climate Model Intercomparison Project phase 5 (CMIP5). Therefore, it is very important to understand clouds and their feedback to climate systems. Generally, the models are supposed to be as close to the nature as possible for the real simulation results, which will, however, lead to the situation in which the models sometimes are too complicated to fully understand. In this case, it is of great help to employ the simple models to investigate the key mechanisms behind the various phenomena. In this chapter, we will make use of Isca to design some simple experiments investigating the zonal mean surface temperature change especially polar amplification of surface temperature change in aquaplanet simulations.

1.1.2 Polar amplification

Polar amplification is the phenomenon where surface temperature in polar region rises faster than the global average [IPCC, 2007], which exists not only in observation where Arctic warming is evident [Johannessen et al., 2004; Polyakov et al., 2002], but also confirmed by models at varying levels of complexity [e.g., Alexeev et al., 2005; Langen and Alexeev, 2007; Merlis and Henry, 2018; Winton, 2006].

Many discussions have focused on the sea ice and surface albedo feedback when discussing the mechanisms of polar amplification under global warming, as it is obvious that initial warming will melt the sea ice in Arctic region, leading to the decrease of surface albedo, which in turn will lead to the absorption of more solar radiation and cause the retreat of sea ice cover in further [Serreze and Barry, 2011]. In fact, diminishing sea ice does play a leading role in recent Arctic temperature amplification [Screen and Simmonds, 2010]. Nevertheless, polar amplification also occurs in simulations even without sea ice and surface albedo feedbacks [e.g., Alexeev et al., 2005; Cai, 2005, 2006; Langen et al., 2012]. Different physical mechanisms

have been proposed to explain polar amplification, including increasing northward heat transport [Alexeev et al., 2005] and climate feedbacks such as Planck feedback, lapse rate feedback, cloud feedback and water vapor feedback [Pithan and Mauritsen, 2014; Screen and Simmonds, 2010; Vavrus, 2004]. In addition, these mechanisms will interact with each other in the climate system, making the quantification of the contributions to polar amplification more complicated. For instance, Graversen and Wang [2009] found that an increase of water vapor and total cloud cover is favorable for a stronger greenhouse effect in the Arctic than at lower latitudes with fixed albedo under doubled CO_2 forcing. However, Screen and Simmonds [2010] find no evidence of changes in cloud cover contributing to recent near-surface Arctic warming.

Goosse et al. [2018] categorized the feedbacks in polar region into radiative and non-radiative feedbacks, in which the first linked the surface temperature change to the perturbation of top of the atmosphere (TOA) energy budget and the latter one is associated with sea ice, the ocean and other components of climate system. In fact, radiative feedback analysis can provide relative clear insights into the mechanisms of surface temperature change at high latitudes, and thus we focus on radiative feedback analysis only in this study. Besides surface albedo feedback, various feedback processes in climate system can also contribute to the polar amplification. Compared to regions with higher background temperature, a given increase in emitted radiation requires a larger temperature increase at colder regions according to Stefan-Boltzman law, indicating that Planck feedback (i.e., feedback related to uniform warming in surface and tropsphere) supports polar amplification naturally [Pithan and Mauritsen, 2014].

The lapse rate feedback, associated with vertically non-uniform warming of atmosphere, is negative in tropical region as the vertical temperature profile is close to moist adiabatic. It is positive in polar regions due to the larger static stability, leading to 'top-heavy' and 'bottom-heavy' warming profiles in tropical and polar regions respectively [Graversen and Wang, 2009; Kim et al., 2018; Manabe and Wetherald, 1975; Pithan and Mauritsen, 2014].

As for the water vapor feedback, the increased water vapor will amplify the greenhouse effect and cause further warming, and is bigger in tropical regions as the increase of water vapor is greater there [Pithan and Mauritsen, 2014; Taylor et al., 2013]. In fact, the quantification of the relative importance of these contributions is difficult. For example, Pithan and Mauritsen [2014] pointed out that temperature feedback is the largest contribution and the surface albedo feedback is the second main contributor to Arctic amplification, which is, conversely, cited as the largest contributor in some studies [e.g., Hall, 2004; Manabe and Wetherald, 1975; Winton, 2006].

In this chapter, we will revisit the polar amplification problem with Isca model as it provides variety of options to configure experiments. For instance, it is a good chance to examine the roles of water vapor as Isca has provided radiation schemes with/without water vapor feedback.

1.2 Experimental Setups

The Isca model is employed for the simulations. The configuration has 25 vertical levels and is run with spectral dynamical core at T42 horizontal resolution, roughly equivalent to 2.8 degrees in latitude and longitude. The atmosphere is coupled to a slab ocean with a depth of 10m. Oceanic heat transport is prescribed with symmetric Q-flux with respect to equator. The insolation conditions for all the experiments are perpetual equinox without seasonal change but with diurnal variations, because the perpetual equinox insolation can cause the most evident polar amplification compared to the seasonal and annual-mean insolations [Kim et al., 2018]. Three radiation schemes (i.e. BOG, Frierson and RRTM schemes) are applied in our experiments to calculate the radiative transfer, as BOG and Frierson schemes are relative simple gray radiation schemes and RRTM is a widely used full radiation scheme, which can provide a good reference for the results. The sea ice formation is not enabled in the model even if the surface temperature is below the freezing point. Furthermore, the global uniform albedo is adopted in the model, and thus the surface albedo feedback is disabled. The default CO_2 concentration is 360 ppm.

All the experiments are run for 20 years following 10 years of spinup.

1.2.1 Changing forcing through varying albedos

The general way to investigate climate sensitivity is to evaluate the degree of warming in response to a doubling of the CO_2 concentration in the climate system. Actually, the external forcing can be introduced into climate system through other ways such as adding a ghost forcing arbitrarily at the TOA [Alexeev et al., 2005; Hansen et al., 1997]. Given the fact that there is no sea ice in our experiments, changes of albedo will not introduce albedo feedbacks to the climate system. Instead, it provides an simple way to perturb the radiation balance at the TOA without doubling CO_2 concentration. Therefore, we will first examine the zonal mean surface temperature change when varying the albedo. Specifically, four albedos, α =0.27, 0.3, 0.33 and 0.38, are selected for each radiation scheme in this study, where the $\alpha = 0.3$ is roughly the Earth's global averaged albedo and used in the control run for each radiation scheme. $\alpha = 0.27$ (0.33) decreases (increases) 10% from the control run value, which will cause the warming (cooling) response to the climate system. $\alpha = 0.38$ increases even more than the albedo in the control run, leading to a much colder climate state. The experiments for BOG, Frierson and RRTM radiation schemes with different albedos are shown in Table 1.1.

Table 1.1 The experiments for BOG, Frierson and RRTM radiation schemes with four different albedos, where 1× indicates the CO_2 concentration is not doubled.

Albedo Scheme	0.38	0.33	0.3*	0.27
BOG	1×	1×	1×	1×
Frierson	1×	1×	1×	1×
RRTM	1×	1×	1×	1×

* indicates the control run for each radiation scheme.

To estimate the external forcing after changing the albedos, the fixed sea surface temperature (SST) forcing method is applied in this study [Feldl and Roe, 2013a; Hansen et al., 2005; Kim et al., 2018], which has included the adjustment throughout the atmosphere (Figure 1.1d). For each radiation scheme, the radiative forcing for experiments after changing albedos ($\alpha = 0.27, 0.33$ and 0.38) is calculated from

radiation imbalance at TOA when prescribed with the monthly mean SST profiles from control experiment.
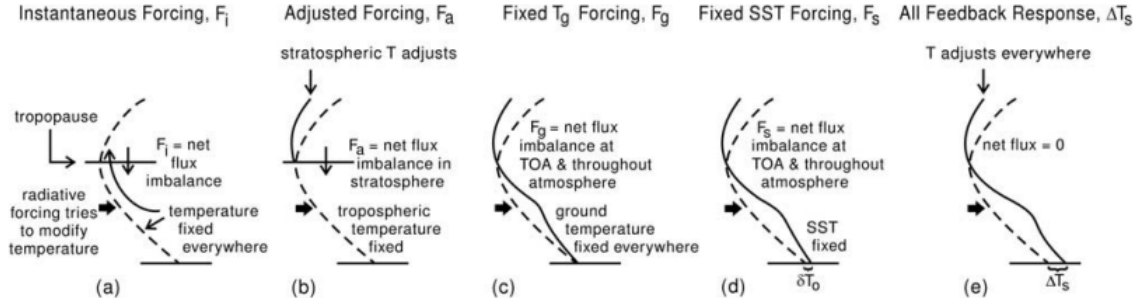

Figure 1.1 Cartoon comparing (a) F_i, instantaneous forcing, (b) F_a, adjusted forcing, which allows stratospheric temperature to adjust, (c) F_g, fixed T_g forcing, which allows atmospheric temperature to adjust, (d) F_s, fixed SST forcing, which allows atmospheric temperature and land temperature to adjust, and (e) ΔT_s, global surface air temperature calculated by the climate model in response to the climate forcing agent. Adapted from Figure 2 of Hansen et al. [2005].

1.2.2 Water vapor feedback in radiation scheme

To examine the roles of water vapor feedback in polar amplification, the BOG and Frierson radiation schemes are employed in this study as only one of the schemes provides moisture feedback. According to Byrne and O'Gorman [2013] and Frierson et al. [2006], the same shortwave radiation schemes are adopted in both schemes, but the ways to calculate the longwave radiation transfer are different. Specifically, the longwave optical thickness (τ) for BOG scheme in Isca is

$$\frac{\mathrm{d}\tau}{\mathrm{d}\sigma} = a\mu + bq + c\log(CO_2/360), \tag{1.1}$$

where $\sigma = p/p_0$, and p_0 is 10^3 hPa; q is the specific humidity and $\mu = 1$ is a scaling parameter intended to represent absorption by well-mixed gases; $a = 0.1627$, $b = 1997.9$, $c = 0.17$ are values recommended in Vallis et al. [2018]. $CO_2 = 360$ ppm is the default CO_2 concentration, which has no effect on changes in longwave optical thickness at this default level. It is evident that water vapor feedback can have a influence on the optical depth in the BOG radiation scheme. However, longwave optical depth in Frierson scheme is a function of latitude (θ) and pressure (p) [Frierson et al., 2006], which is specified to approximate the effects of atmospheric

water vapor. The surface value of optical depth (τ_0) is given in the form of

$$\tau_0 = \tau_{0e} + (\tau_{0e} - \tau_{0p}) \sin^2 \theta, \qquad (1.2)$$

where τ_{0e} and τ_{0p} are the surface optical depth at equator and pole separately. The vertical structure of optical depth (τ) is a combination of a linear term, which is included to reduce stratospheric relaxation times, and a quartic term, which is used to approximate the structure of water vapor in the atmosphere as it is an absorber with a scale height that is one quarter of the pressure scale height, and thus is given by

$$\tau = \tau_0 \left[f_l \frac{p}{p_s} + (1 - f_l) \left(\frac{p}{p_s} \right)^4 \right], \qquad (1.3)$$

where p_s is sea level pressure and coefficient f_l is set to 0.1 in the equation. Noting that moisture is held fixed in Frierson scheme, it implies that the comparison between simulation results from BOG and Frierson schemes can demonstrate the role of water vapor feedback in polar amplification. To investigate that role in further, we re-run the experiments for BOG scheme without allowing water vapour feedback by prescribing the annual and zonal mean specific humidity profiles from the control run. In this case, the processes such as water vapour advection and convection will carry on as usual, but the moisture feedback is turned off. All the associated results will be shown in Section 1.4.

1.2.3 Climate feedbacks

In order to quantify the relative importance of various contributions to polar amplification, the radiative kernel technique [Shell et al., 2008; Soden et al., 2008] is used to calculate various climate feedbacks (see Section 1.3). In general, climate feedback is used to characterize the response of climate system to an external radiative forcing, which can either amplify or diminish the effect of the forcings [Hansen et al., 1984]. Specifically, a feedback that can increase the initial climate changes is called a positive feedback, while the one that can reduce the initial changes is a negative feedback. The change of net radiative flux at TOA between two different climate

states, ΔR, can be represented by

$$\Delta R = \Delta \mathscr{F} + \lambda \Delta T_s + \mathcal{O}\left(\Delta T_s^2\right), \qquad (1.4)$$

which can be viewed as a Taylor expansion in surface temperature change (ΔT_s) [Feldl and Roe, 2013b]. The first term, $\Delta \mathscr{F}$, in Eq. (1.4) is the climate forcing, which is estimated by the fixed-SST method [Feldl and Roe, 2013b; Hansen et al., 2005; Kim et al., 2018] as shown in Figure 1.1. The second term, $\lambda \Delta T_s$, reflects the radiative flux change that is linearly depend on the surface temperature change, and λ is the total *feedback parameter*. The third term (or residual term) $\mathcal{O}\left(\Delta T_s^2\right)$ represents the high-order components, reflecting the non-linear interactions among different processes, which we consider to be neglected in our analysis. It should be pointed out that variables in Eq. (1.4) can be a global mean value or a function of the latitude [Feldl and Roe, 2013b]. When neglecting the nonlinearities and interactions among the feedbacks, the feedback parameter λ can be decomposed into the sum of different components:

$$\lambda = \lambda_T + \lambda_w + \lambda_\alpha + \lambda_C, \qquad (1.5)$$

where λ_T, λ_w, λ_α and λ_C are the feedback parameters related to temperature, water vapor, surface albedo and cloud, respectively. In further, the temperature feedback can be divided into Planck feedback (λ_P) and lapse rate feedback (λ_L) [Soden and Held, 2006], that is $\lambda_T = \lambda_P + \lambda_L$, where the Planck feedback assumes that the tropospheric temperature change is vertically uniform and equals to the surface temperature change (in other words, there is no vertical temperature change in the troposphere) and the lapse rate feedback is associated with the vertical temperature change in troposphere that deviates from the surface temperature change [Bony et al., 2006; Feldl et al., 2017; Soden and Held, 2006]. In our analysis, the cloud feedback (λ_C) is automatically neglected as there is no cloud scheme in Isca model currently. The calculation of these feedbacks for Isca model is described in Section 1.3 and the analysis of the contributions to polar amplification from these feedbacks will be presented in Section 1.4.

1.3 Method

1.3.1 Radiative kernel method

In this study, we apply radiative kernel technique [Shell et al., 2008; Soden et al., 2008] to calculate the climate feedbacks of Isca model. It should be mentioned that radiative kernel technique is not the only approach to quantify climate feedbacks, other methods such as partial perturbation radiative (PRP) method [Wetherald and Manabe, 1988], regression method of Gregory [2004] are also used by other studies. Nevertheless, the PRP method is time consuming and the calculations have to be repeated for different simulations [Shell et al., 2008]. Furthermore, the interpretation of the results must be cautious for the possible problem associated with correlated variables as pointed by Bony et al. [2006]. In contrast, the radiative kernels are calculated from the offline version radiative codes and can be used for different experiments and models. For instance, Soden et al. [2008] compare the climate feedbacks in 14 different coupled ocean-atmosphere models from the Fourth Assessment of the Intergovernmental Panel on Climate Change (IPCC AR4) with radiative kernels from three different general circulation models (GCMs) respectively, demonstrating that the strength of global feedbacks is relative insensitive to the choice of kernels (Figure 1.2).

To get the radiative kernels for one model, the model should produce high-frequency (typically either every time step or every 3 hours) output in order to get the instantaneous fields for various variables we needed. Initially, the model is performed with profiles without perturbation in order to get the original TOA radiation fluxes, then run with profiles where certain variable is disturbed at each level and each time step (e.g. 3 hours) to obtain the new TOA radiation fluxes corresponding to that perturbation. Specifically, the small perturbations are applied to surface temperature (+1 K), atmospheric temperature (+1 K) and specific humidity (the change amount is determined when temperature increases by 1 K but assuming relative humidity is constant) at each vertical level at each time step (e.g. 3 hours), respectively. In particular, the change of specific humidity Δq for one layer is given
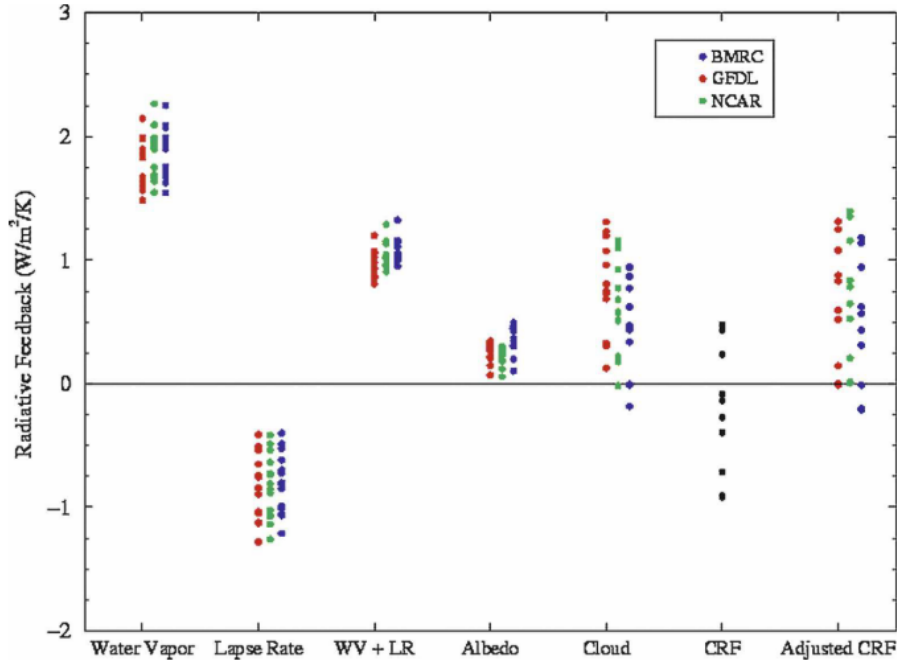
Figure 1.2 The global-mean water vapor, lapse rate, water vapor+lapse rate, surface albedo, and cloud feedbacks computed for 14 coupled oceanatmosphere models (listed in Table 1 of Soden and Held [2006]) using the GFDL (red), NCAR (green), CAWCR (blue) kernels. Adapted from the Figure 7 of Soden et al. [2008].

by

$$\Delta q = q \left(\frac{e_s(T+1)}{e_s(T)} - 1 \right), \tag{1.6}$$

where q, e_s, T are specific humidity, saturation pressure of water vapor and temperature respectively, and e_s satisfies ClausiusClapeyron relation, i.e. $\frac{de_s}{dT} = \frac{L_v e_s}{R_v T^2}$, where L_v is the specific latent heat of evaporation of water, taken to as a constant value of 2.5×10^6 J kg^{-1} K^{-1}; R_v, with value of 461.5 J kg^{-1} K^{-1}, is the gas constant of water vapor. The simple method used in this study to estimate the saturated water vapor pressure is

$$e_s(T) = e_{s0} \exp \left[\frac{L_v}{R_v} \left(\frac{1}{T_0} - \frac{1}{T} \right) \right], \tag{1.7}$$

where e_{s0} is a reference value of 6.1078 hPa for this at a reference temperature $T_0 = 273.16$ K. After each perturbation, the changes of radiation flux at TOA are recorded and then averaged over each month to get the kernels. In fact, the traditional kernels are supposed to compute under total-sky and clear-sky conditions separately so as to obtain the radiative effect of clouds, but only clear-sky case will be calculated for Isac model at present due to the lack of cloud schemes.

If ΔR represents the TOA radiation flux change due to the perturbation of vari-

able x, then the radiative kernel for each level is defined as $K_x^i = \partial R/\partial x_i$, which is a function of space and time. In general, the resulting kernels are weighted relative to 100-hPa thick layer in order to make it easier to compare with other different kernels, that is $\mathbb{K}_x^i = K_x^i/\Delta p_i \times 100$ hPa, where Δp_i is the thickness of layer i in units of hPa. The total radiation flux change at TOA due to x perturbation is obtained by integrating from the surface to the tropopause, that is $\Delta R = \sum_{i=1}^{nlev} \frac{\partial R}{\partial x_i} \Delta x_i$, where $nlev$ denotes the number of vertical levels. The tropopause height is determined following the approach developed by Soden and Held [2006], which defines the tropopause (H) at 100 hPa at the equator and 300 hPa at the poles and varies by cosine of latitude (ϕ) in between, that is $H = 300 - 200 \cos \phi$. After getting the radiation response, the climate feedback parameter is defined as

$$\lambda = \frac{\Delta R}{\Delta T_s} = \frac{1}{\Delta T_s} \sum_{i=1}^{n} \frac{\partial R}{\partial x_i} \Delta x_i, \qquad (1.8)$$

where ΔT_s is the surface temperature change and the units of λ is Watt per meter squared per Kelvin (Wm^{-2} K^{-1}). Noting that zonal-mean variables, not the global-mean values, will be applied in Eq. (1.8) if we analyze local or regional feedback, as it can offer some advantages such as spatial pattern of changes [Feldl et al., 2017; Feldl and Roe, 2013a].

In calculation of different climate feedbacks, different variables (x) will be employed in Eq. (1.8). As for Planck feedback, the temperature change is vertically uniform in atmosphere, meaning that the air temperature change equals to the surface temperature change, so we have $x = T_s$ in Eq. (1.8). Similarly, the lapse rate feedback is associated with the warming/cooling that deviates from surface temperature change, indicating that $x = T_a - T_s$ (T_a denotes the atmospheric temperature) is utilized in Eq. (1.8). Regarding to the water vapor feedbacks, the natural logarithm of atmospheric specific humidity (i.e. $x = \ln q$) is applied in Eq. (1.8), since the absorption of radiation by water vapor is approximately proportional to the natural logarithm of water vapor content [Feldl and Bordoni, 2016; Liu et al., 2018; Shell et al., 2008]. Similarly, Huang et al. [2017] employ another way to calculate the water vapor feedback:

$$\lambda_w = \sum_i^{nlev} K_q^i \frac{\Delta \ln q_i}{(\delta \ln e_s / \delta T)_i} \frac{1}{\Delta T_s}, \tag{1.9}$$

and $(\delta \ln e_s)_i$ is estimated by $(e_s(T_i + 1) - e_s(T_i)) / e_s(T_i)$, which is similar to the method that Pendergrass et al. [2018] used to calculate the water vapor kernel (refer to the scripts on https://github.com/apendergrass/cam5-kernels), and hence we use Eq. (1.9) to calculate the water vapor kernel in this study.

1.3.2 Radiative kernels in Isca

To calculate the radiative kernels for Isca, a 10-year control experiment ($\alpha = 0.3$) is re-run for each radiation scheme to get corresponding model outputs (e.g. temperature, specific humidity) at 3-hour frequency. Then 1-year climatology computed from the last 5-year period is taken as the basic profiles for the offline radiation codes. Then the perturbation procedure will be carried out for different variables such as surface temperature, temperature and specific humidity to obtain the surface temperature, temperature and water vapor kernels respectively. The radiative kernel results for each radiation scheme are shown below.

Frierson and BOG scheme

The radiative kernels for temperature, water vapor and surface temperature in BOG schemes are shown in Figure 1.3, but there is no water vapor kernel in Frierson scheme (Figure 1.4). The temperature kernel illustrates the contribution of different latitudes and levels to the change of TOA longwave fluxes, where the numerical values are generally negative, indicating that an increase in temperature increase the the outgoing longwave radiation. As shown in Figure 1.3a and Figure 1.4a, the values of temperature kernels are more negative in tropical atmosphere owing to the larger sensitivity according to the Stefan-Boltzmann law, but the location of largest sensitivity is somewhat different from the temperature kernel in RRTM scheme (Figure 1.5a), where the largest sensitivity also appears in bottom at tropical region. Low sensitivity occur near the tropopause and polar region in BOG's and Frierson's temperature kernel, reflecting the regional differences in lapse rate and emissivity
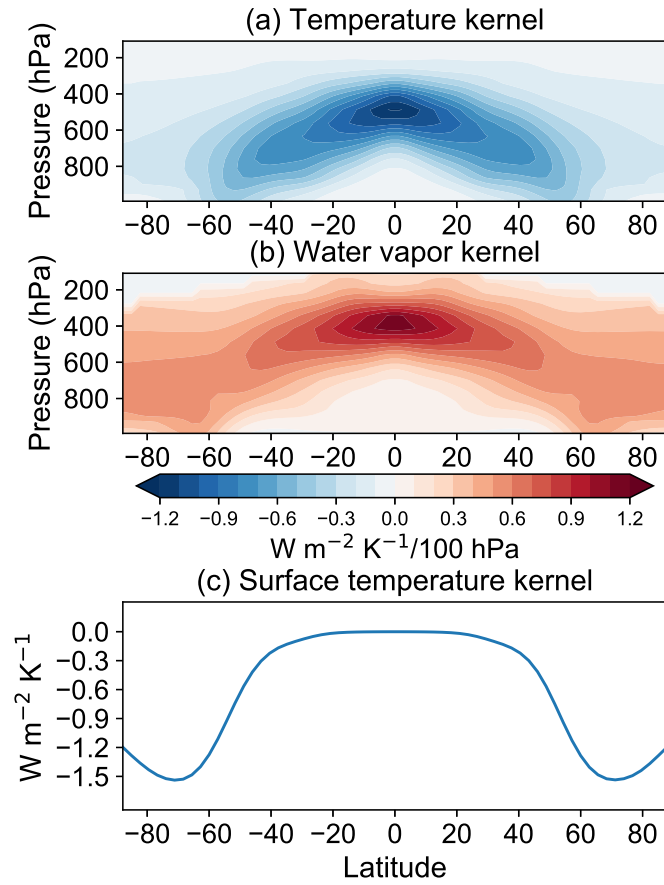
Figure 1.3 Annual-mean and zonal-mean radiative kernel for BOG radiation scheme: (a) temperature kernel with respect to 1-K increase in atmospheric temperature, (b) water vapor kernel for a specific humidity perturbation corresponding to a 1-K temperature increase with relative humidity unchanged, (c) surface temperature kernel for 1-K perturbation in surface temperature.
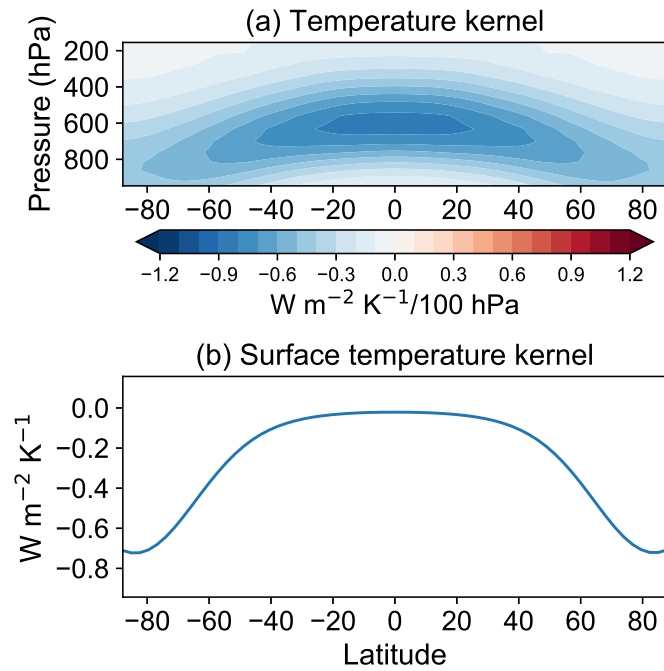

Figure 1.4 As in Figure 1.3, but only for temperature and surface temperature kernels in Frierson radiation scheme.

[Soden et al., 2008]. The vertically integrated global, annual mean of temperature kernel for BOG and Frierson radiation schemes are -3.45 and -3.65 W m^{-2} K^{-1} respectively, which are similar to clear-sky temperature kernel for Geophysical Fluid Dynamics Laboratory (GFDL) atmospheric model (version AM2p12b), which is 3.6 W m^{-2} K^{-1} estimated by Soden et al. [2008].

As for the water vapor kernel for BOG scheme (Figure 1.3b), which demonstrate the relative importance of different level and latitudes to the strength of longwave water vapor feedback when temperature increases uniformly but the relative humidity keeps unchanged. In contrast, the values for water vapor feedback are positive almost everywhere, as the increase in the content of water vapor in atmosphere can help to increase the net incoming longwave radiation at TOA. Clearly, the water vapor kernel is largest in deep tropics and decreases in poleward direction. The vertically integrated global and annual mean for water vapor kernel in BOG scheme is 3.61 W m^{-2} K^{-1}, which is more than twice of clear-sky water vapor kernel (1.62 W m^{-2} K^{-1}) of GFDL AM2p12b [Soden et al., 2008], suggesting that the water vapor feedback is much stronger in BOG scheme.

The surface temperature kernel also contributes partially to the temperature feedback (the Planck feedback), and the warming of surface temperature increase the outgoing longwave radiation, so the surface temperature kernel are negative in all the latitudes as displayed in Figure 1.3c and Figure 1.4b. But the scales of surface temperature kernel in BOG and Frierson radiation schemes are different, and the possible reason for that is the surface temperature came from their own control runs rather than the same ones.

RRTM scheme

The offline version of RRTM code is from *pyrrtm* (https://github.com/tomflannaghan /pyrrtm), which provides an user-friendly python wrapper for the single-column version of RRTM scheme. The input profiles for *pyrrtm* are from the Isca outputs in which the albedo is 0.3. Nevertheless, one frustrating fact is that the single-column version of RRTM will consume too much time if we perturb each level and each
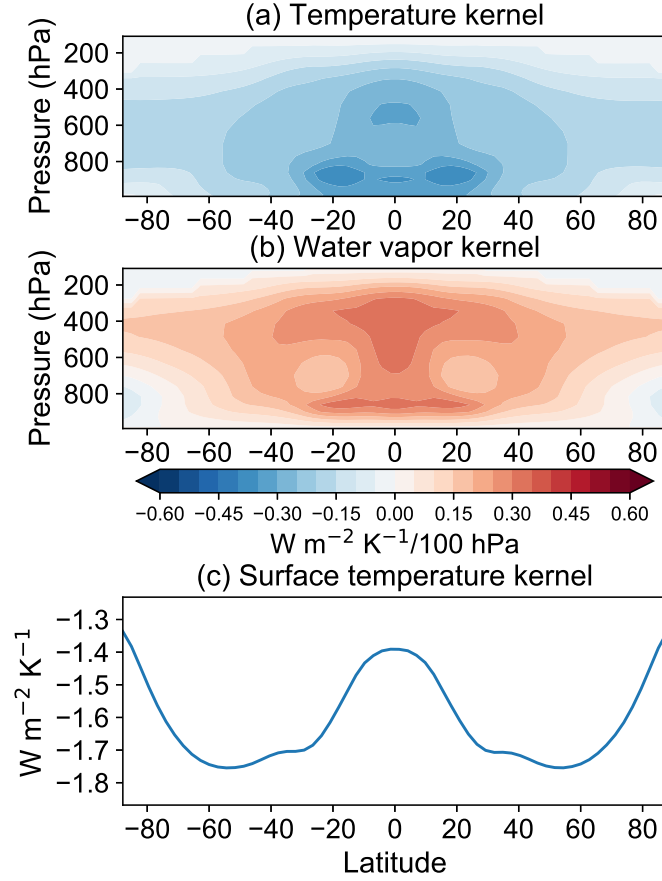
Figure 1.5 As in Figure 1.3, but for RRTM radiation scheme.

position every 3 hours. In order to get over this drawback, we employ zonal-mean and monthly mean profiles as the input for the *pyrrtm* to calculate the radiative kernels. As shown in Figure 1.5a, the temperature kernel for RRTM is weaker compared to the results of GFDL AM2.1 (Figure 1.6a) computed by Feldl et al. [2017], and the vertical integration of global and annual mean result is -1.79 W m^{-2} K^{-1}, which is almost a half of the clear-sky results (-3.6 W m^{-2} K^{-1}) of GFDL AM2p12b [Soden et al., 2008], suggesting that the feedbacks depend on this kernel would be small than other GCM's. However, the RRTM surface temperature kernel makes the situation different, which has the similar shape but the strength is much stronger compared to the surface temperature kernel of GFDL AM2.1 (Figure 1.6d), making the Planck feedback for RRTM is reasonable (Figure 1.7c). With respect to water vapor kernel for RRTM, the vertical integration of global and annual mean value is 1.65 W m^{-2} K^{-1}, which is close to the longwave water vapor kernel results (1.62 W m^{-2} K^{-1}) of GFDL AM2p12b, meaning that the water vapor kernel is sensible.

Although the positive values dominate the water vapor kernels, some negative values appear in polar region as there are temperature inversions near the surface at high latitudes, which will decrease, rather than increase, the net longwave flux in response a increase of water vapor [Soden et al., 2008]. However, this doesn't occur in water vapor kernel for BOG radiation scheme (Figure 1.3b).
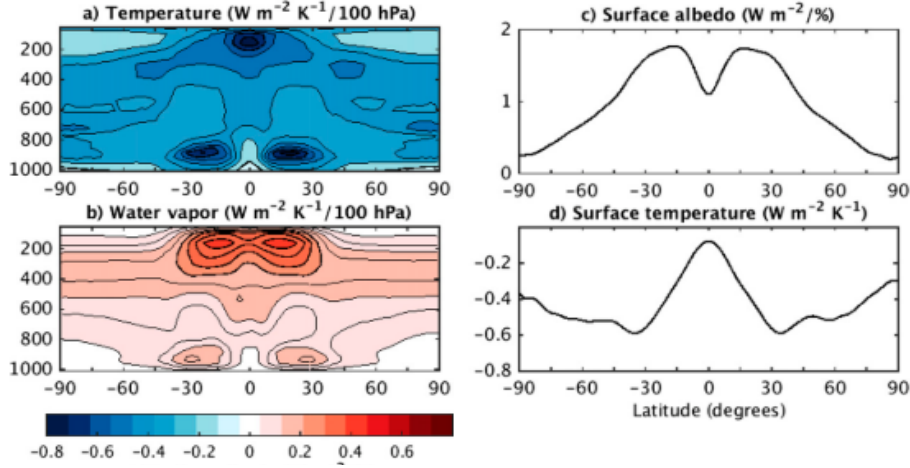

Figure 1.6 Annual-mean, zonal-mean radiative kernels for the GFDL AM2.1 aquaplanet based on a $4\times$ CO_2 simulation with daily mean solar zenith angle: (a) temperature kernel [W m^{-2} K^{-1} / 100 hPa], (b) water vapor kernel for a specific humidity perturbation corresponding to a 1-K temperature in- crease and fixed relative humidity, (c) surface albedo kernel, and (d) surface component of the temperature kernel. (Adapted from Figure A1 of Feldl et al. [2017])
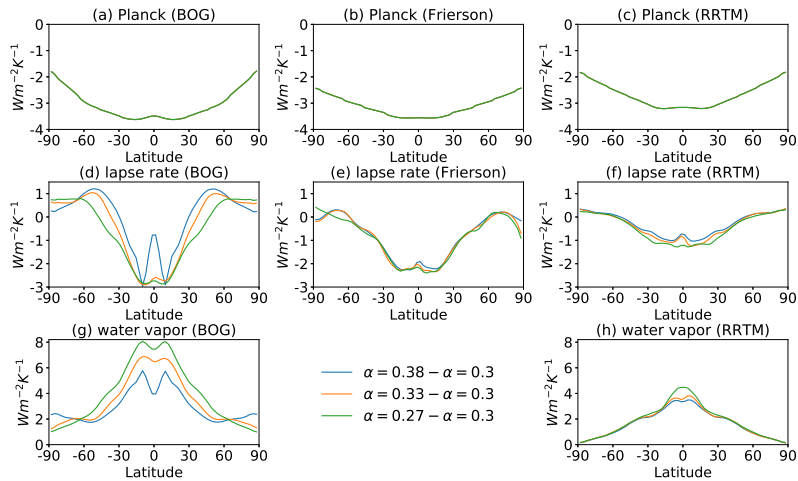

Figure 1.7 The zonal and annual mean climate feedback parameters for all the experiments in BOG, Frierson and RRTM radiation schemes, where (a)-(c) are for the Planck feedbacks, (d)-(f) for the lapse rate feedbacks and (g)-(h) for the water vapor feedbacks. Blue, orange and green lines represent the experiments when albedo (α) is changed from 0.3 to 0.38, 0.33 and 0.27 respectively.

1.3.3 Climate feedbacks in Isca

For each radiation scheme, albedo parameter is changed from 0.3 to 0.27, 0.33 and 0.38 to provide an external forcing to the simulation respectively, leading to different degree of climate responses in experiments. Thus in this section, we will use the radiative kernel technique to analyze the feedbacks for these experiment when changing albedos and the resulting Planck feedback, lapse rate feedback and water vapor feedback for each experiments are displayed in Figure 1.7.

Table 1.2 Global mean lapse rate feedback parameters (Units: W m^{-2} K^{-1}).

Experiment	BOG	Frierson	RRTM
$\alpha = 0.38 - \alpha = 0.3$	-0.33	-1.23	-0.51
$\alpha = 0.33 - \alpha = 0.3$	-0.84	-1.28	-0.61
$\alpha = 0.27 - \alpha = 0.3$	-1.15	-1.32	-0.72

Table 1.3 Global mean water vapor feedback parameters (Units: W m^{-2} K^{-1}).

Experiment	BOG	RRTM
$\alpha = 0.38 - \alpha = 0.3$	3.38	2.14
$\alpha = 0.33 - \alpha = 0.3$	4.21	2.23
$\alpha = 0.27 - \alpha = 0.3$	5.03	2.41

The Planck feedback is negative in all latitudes (Figure 1.7a-c), meaning that an increase in temperature can increase the outgoing longwave radiation. In addition, the strength of Planck feedback in polar region is weaker than the tropical region due to smaller blackbody emissions per unit warming at lower temperatures according to Stefan-Boltzmann law [Goosse et al., 2018]. The strengths of Planck feedback for three different experiments in each radiation scheme almost have no difference to each other. What's more, the global mean Planck feedback parameters are -3.82, -3.79 and -3.41 W m^{-2} K^{-1} for BOG, Frierson and RRTM radiation schemes respectively, showing that the differences of Planck feedbacks in different radiation schemes are small. Regarding to the lapse rate feedbacks, they are negative in low latitudes but positive in high latitudes, which is due to the different vertical distribution of temperature change in polar region compared to the tropics, as the temperature change is bottom heavy in polar regions [Pithan and Mauritsen,

2014]. The global mean lapse rate feedback parameters for all experiments and all radiation schemes are listed in Table 1.2. It is clear that the variance of global mean lapse rate feedbacks among different radiation schemes is large, but is small within the experiments with same radiation schemes, except the one where albedo is 0.38 in BOG radiation scheme. As for water vapor feedback, it is positive in all experiments, implying that the net longwave radiation increase in response to temperature warming. However, the spatial distribution of water vapor feedback is nonuniform, with high feedback in tropics but small values in polar region (Figure 1.7g and 1.7h) because of the nonlinear effect of water vapor in response to warming. In addition, the global mean water vapor feedback parameters are displayed in Table 1.3, where the water vapor feedback in BOG schemes is almost twice of feedbacks in RRTM scheme and the later is close to the water vapor feedback (2.01 W m^{-2} K^{-1}) estimated by Soden et al. [2008] in GFDL AM2p12b, indicating that the water vapor feedback is much stronger in BOG radiation scheme.
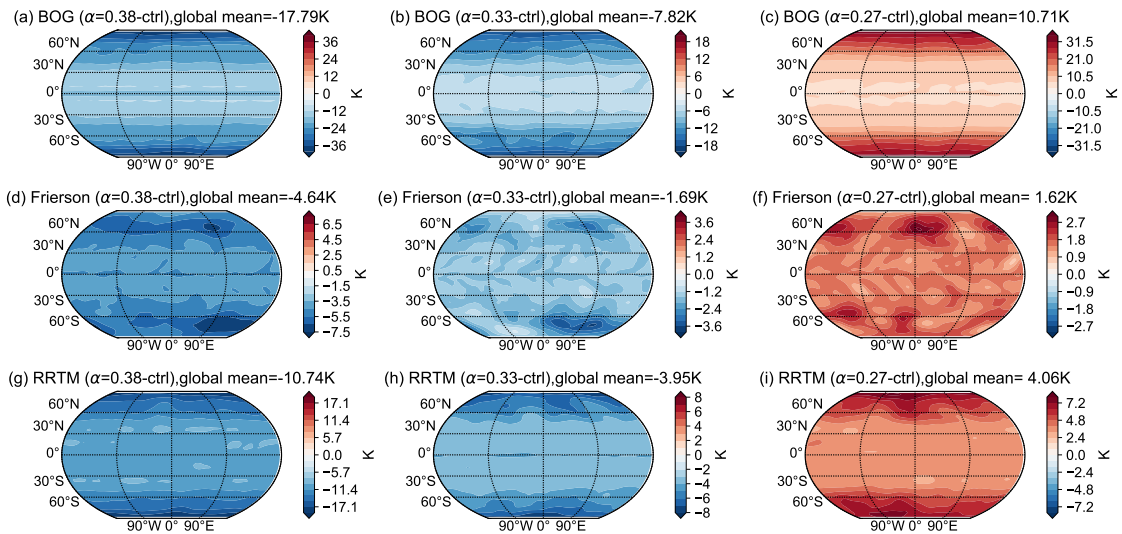
1.4 Results

1.4.1 Surface temperature response

Figure 1.8 The global patterns of annual-mean surface temperature differences between the runs after changing albedos and the control run (i.e. $\alpha = 0.3$) for (a-c) BOG, (d-f) Frierson and (g-i) RRTM radiation schemes respectively, where the (a, d, g) left, (b, e, h) middle and (c, f, i) right panels represent the runs in which albedos are changed from 0.3 to 0.38, 0.33 and 0.27 respectively.

The global patterns of annual mean surface temperature differences after changing albedos for the BOG, Frierson and RRTM radiation schemes are displayed in Figure 1.8, where BOG scheme produces the largest surface temperate changes compared to the other two radiation schemes and Frierson scheme produces the weakest responses. For example, the annual and global mean surface temperature difference is 10.71K in experiment where the albedo decreased 10% from control run (i.e. from 0.3 to 0.27) for BOG scheme, which are, however, only 4.06K and 1.62K for RRTM and Frierson schemes. Despite the responses are in a relative wide ranges, all simulation results from the three radiation schemes show polar amplified patterns either in cooling or warming situations, which are clearly shown in the annual and zonal mean patterns (Figures 1.9a-c). The striking feature is that the strongest polar amplification patterns appear in BOG scheme. However, the zonal mean surface temperature change in Frierson scheme is almost flat with slight amplified cooling or warming at high latitudes but not exactly at the poles. Like the global mean surface temperature changes, the zonal mean patterns and the polar amplification are also moderate in RRTM scheme among the three schemes. To make the feature more evident, the zonal mean surface temperature responses are also normalized by the change in global mean surface temperature (Figures 1.9d-f), showing that results from Frierson scheme also have a slight polar amplification. Generally, the Arctic warming is almost twice as large as the global average in recent decades [Serreze and Francis, 2006]. For example, the Arctic has a warming 1.9 times that of the globe on average in twelve IPCC AR4 models in CO_2 doubling experiments [Winton, 2006]. As for the observed Arctic warming in the last half century, the zonal-mean Arctic warming is roughly 3 times compared to tropical warming [Merlis and Henry, 2018]. All results suggest that the ratios between polar temperature response and global averaged value seem reasonable due to the lack of some feedback mechanisms such as surface albedo feedback in our experiments.

To better understand the surface temperature responses, the structures of vertical atmospheric temperature changes are also investigated. As shown in Figure 1.10, it is obvious that bottom-heavy cooling or warming profiles appear in polar regions
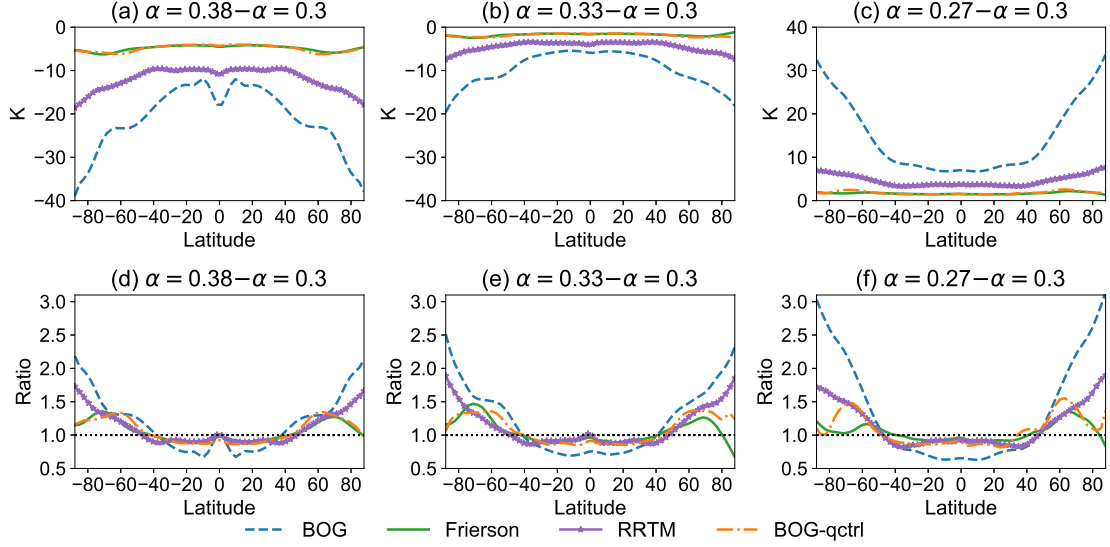
Figure 1.9 The zonal mean and annual mean surface temperature changes for experiments where albedo is changed from 0.3 to (a) 0.38, (b) 0.33 and (c) 0.3 respectively. Correspondingly, (d)-(f) show the ratios of surface temperature change at each latitude to the global mean surface temperature change for different simulations. Each experiment has been run in the BOG (blue dashed line), Frierson (green solid line) and RRTM (purple solid-starred line) radiation schemes respectively. The orange dash-dotted lines denote the experiments in BOG scheme without moisture feedback.
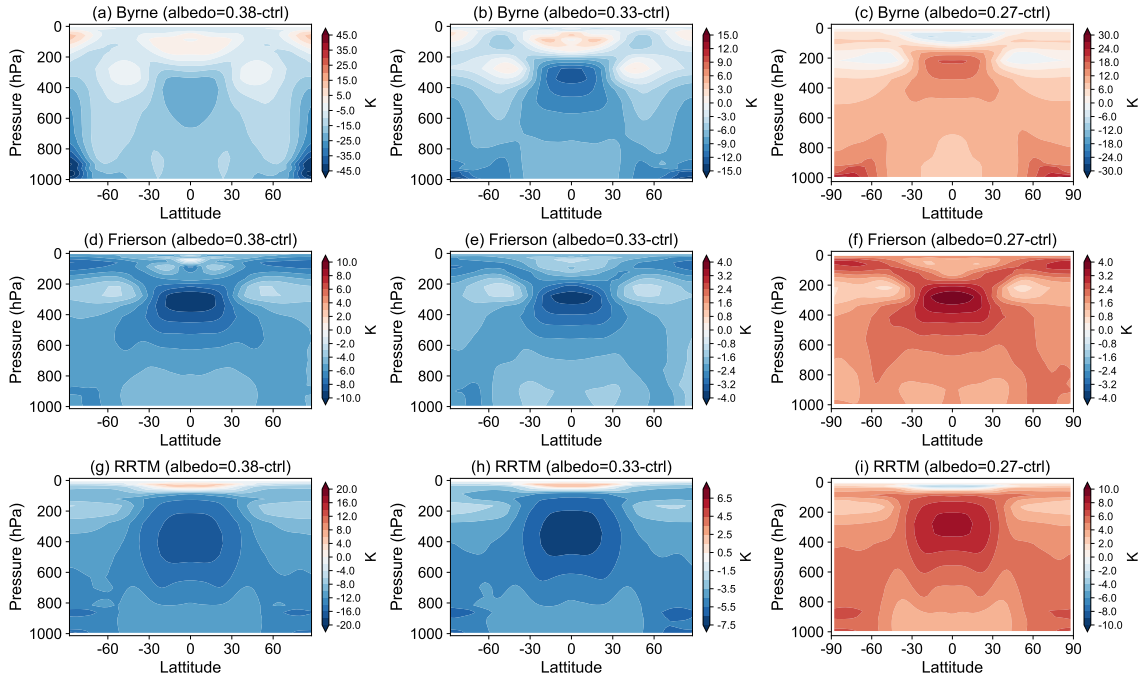

Figure 1.10 The annual mean atmospheric temperature change profiles for experiments in (a)-(c) BOG, (d)-(f) Frierson and (g)-(i) RRTM radiation schemes. The (a, d, g) left, (b, e, h) middle and (c, f, i) right panels are for the experiments where albedos are altered from 0.3 (control run) to 0.38, 0.33 and 0.27 respectively.

(Figures 1.11a-c) in all the experiments, but top-heavy cooling or warming profiles appear in tropical upper troposphere (Figures 1.11d-f). Many studies have found that these bottom-heavy structure is associated with polar amplification [Kim et al., 2018; Park et al., 2018; Pithan and Mauritsen, 2014; Screen et al., 2012], as the stability in polar region can trap more heat at the surface in warming case, which hence leads to the positive lapse rate feedback in polar region (Figures 1.7d-f). In contrast, the lapse rate feedback is negative in tropics, which means that in a warming climate, more latent heat will be released in upper troposphere and thus cause greater warming in the upper troposphere than at the surface [Pithan and Mauritsen, 2014]. It is worth noting that the sea ice is responsible for the stable atmospheric structure in polar region in the real world, but the stability of polar region in our study is due to the equinox solar radiation. Kim et al. [2018] studied the sensitivity of polar amplification to insolation conditions and found that the equinox insolation brings the largest static stability than seasonal or annual mean conditions due to the year-round near zero solar radiation reaching the polar region. Taking the warming case as an example, the active convection in the tropics induces a tight coupling between surface and upper troposphere, and the rising air parcel in warming climate will release more latent heat in upper troposphere, decreasing the moist lapse rate in the end [Graversen et al., 2014]. Instead, the polar region is more stable and mixing with air aloft is harder than in tropics so that more heat is trapped near surface, leaving a bottom heavy temperature structure and positive lapse rate feedback [Pithan and Mauritsen, 2014]. What's more, if we check closely the bottom heavy profile in Frierson scheme, the largest warming or cooling near surface occurs at about 70 degree not the poles (Figure 1.10d-f), which explains largest value of the zonal mean surface temperature change in Frierson scheme in Figure 1.9.

In summary, polar amplification can exist in the aquaplanet model even without the sea ice and surface albedo feedback. Regarding the three radiation schemes we utilized in this study, the polar amplification of surface temperature is strongest in BOG scheme, moderate in RRTM and weakest in Frierson scheme. As mentioned

in Section 1.2.2, the crucial distinction between BOG and Frierson is whether there
is moisture feedback in their longwave radiation schemes, which will be discussed in
further in Section 1.4.2. On the mechanisms about polar amplification, the bottom
heavy structure of temperature difference provides some reasonable explanations for
the polar amplification via lapse rate feedback, which will be investigated further in
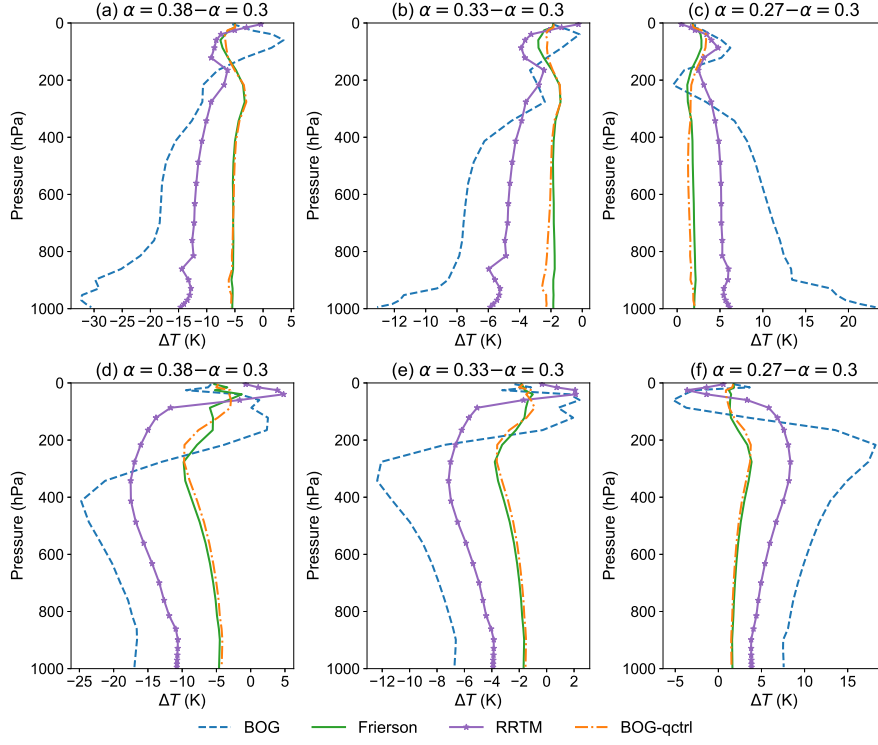Section 1.4.4.

Figure 1.11 The annual mean profiles of atmospheric temperature change in (a-c) polar
(60N northward) and (d-f) tropical (10S-10N) regions, where (a)(d), (b)(e) and (c)(f) are
for the experiments where albedo is changed from 0.3 to 0.38, 0.33 and 0.27 respectively.
The blue dashed, green solid and purple solid-starred lines denote BOG, Frierson and
RRTM radiation schemes respectively. The orange dash-dotted lines denote the experi-
ments in BOG scheme without moisture feedback.

1.4.2 Water vapor feedback

The annual and zonal mean change of moisture profiles from different radiation
schemes are exhibited in Figure 1.12, and it is clear that the change of specific hu-
midity profile is strongest in BOG scheme and mildest in Frierson scheme both in
cooling and warming cases. Noting that the specific humidity increases (decreases)
in warming (cooling) cases almost everywhere but most strongly near the surface at
low latitudes, indicating that the radiative effect of water vapor is strongly amplified
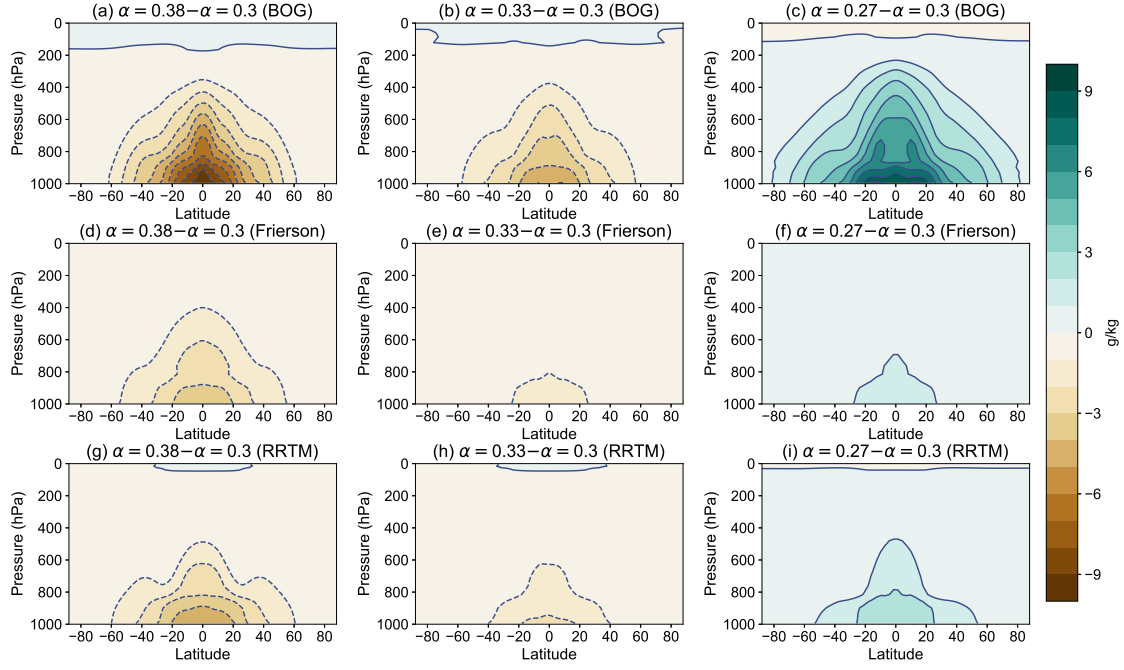
Figure 1.12 As Figure 1.10, but for the specific humidity change in experiments with BOG, Frierson and RRTM radiation schemes.

at low latitudes [Langen et al., 2012; Pithan and Mauritsen, 2014]. However, the previous results show that even if the only difference between the BOG and Frierson radiation schemes lies in whether moisture feedback existing in longwave radiation transfer, the polar amplification of surface temperature change is evident in BOG scheme rather than in Frierson scheme, although there is a weak polar amplified effect in Frierson scheme (Figure 1.9 and Figure 1.10), which implies that water vapor feedback is possibly associated with the stark contrast of surface temperature responses. As demonstrated in previous studies [e.g. Schneider et al., 1999], the variability of clouds and water vapor fields are significant to the simulation of radiation field. It is for this reason that we perform the runs without moisture feedback in BOG scheme.

To identify the role of moisture feedback in BOG radiation scheme, we read the specific humidity (q) profile from the control run (i.e. $\alpha = 0.3$) into other experiments (i.e. $\alpha = 0.38$, 0.33 and 0.27) to make the moisture feedback fixed in longwave radiation transfer. The longwave optical depths are examined first before analyzing the simulation results. For instance, the original optical depth profiles from the two runs where albedos are 0.3 (Figure 1.13a) and 0.38 (Figure 1.13b) show great dif-
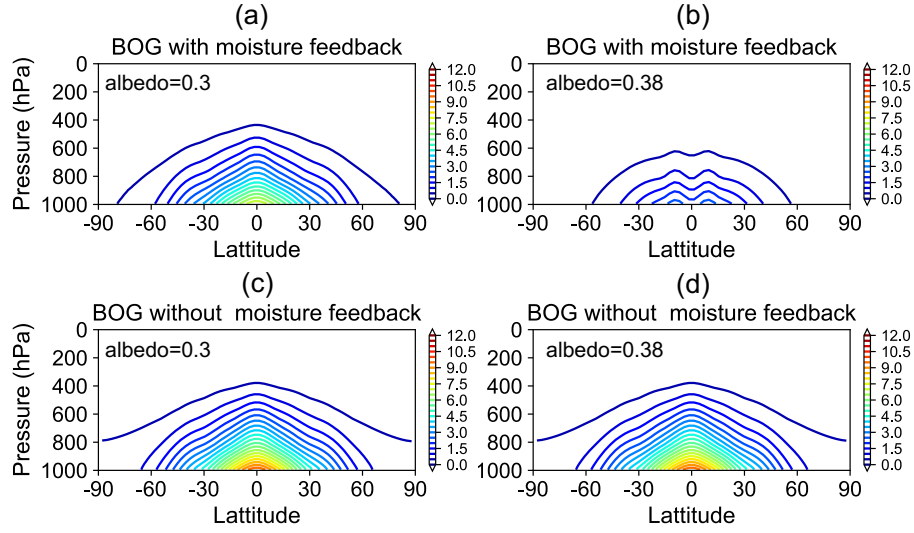
Figure 1.13 Annual and zonal mean longwave optical depth in BOG radiation scheme before and after reading the q profile. (a) and (b) are the averaged longwave optical depth from the experiments with moisture feedback where albedo is 0.3 and 0.38. (c) and (d) are similar to (a) and (b), but the q profiles are fixed by reading annual and zonal mean q profile from control experiment (aledo is 0.3), so (c) and (d) are identical with each other.

ferences when the moisture feedback is freely performed in radiation schemes, but they are almost identical to each other after the specific humidity profile for the run where albedo is 0.38 has been specified by the profile from control experiment (Figure 1.13c and 1.13d). Compared to the original optical depths, the runs with increased the albedos (e.g. $\alpha = 0.38$) have thicker optical depths as they have been prescribed with specific humidity profiles from a warmer control state ($\alpha = 0.3$), where the atmospheric water vapor content is much larger due to the non-linear effect of saturation water vapor pressure with respect to temperature according to Clausius-Clapeyron relation. Similarly, the runs with decreased albedos will have a thinner optical depth as they are specified with moisture profiles from relative cold control state.

The surface temperature change for BOG radiation scheme without moisture feedback (BOG-qctrl, orange dash-dotted lines in Figure 1.9) shows totally different behaviors from the runs with water vapor feedback, where the zonal mean surface temperature changes get much smaller and polar amplification becomes much weaker compared to the original runs, indicating that the moisture feedback plays an important role in the surface temperature change as well as polar amplification at least in BOG scheme. Note that the surface temperature changes in the runs without

moisture feedback in BOG scheme are close to those in Frierson scheme, which is reasonable as moisture feedback is also missing in Frierson scheme. In addition, the vertical temperature profiles in polar and tropical regions also change a lot when there is no water vapor feedback in BOG scheme. Specifically, the bottom-heavy cooling or warming profiles become less evident in polar region (see the orange dash-dotted lines in Figures 1.11a-c) and the top-heavy cooling or warming profiles get weaker in tropical region (orange dash-dotted lines in Figures 1.11d-f), implying the positive lapse rate feedback is weakened in polar region.
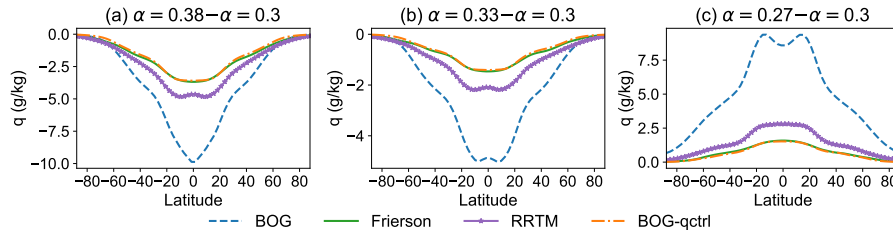

Figure 1.14 As in Figure 1.9, but for the specific humidity at surface.

As remarked by Pithan and Mauritsen [2014], the water vapor feedback contributes more to the tropical warming than to polar warming, which corresponds to our findings for BOG radiation scheme (Section 1.4.4). But we should also notice that while water vapor feedback does not result in polar amplification by itself, it could approximately double the climate sensitivity both at low and high latitudes [Langen et al., 2012]. However, we find the polar amplification of surface temperature decreases remarkably after turning off the water vapor feedback, which as illustrated in Figure 1.14 (blue dashed and orange dash-dotted lines), is due to the water vapor content and its meridional gradient have changed evidently when the moisture feedback is turned off. In addition, the zonal mean profile from BOG scheme with moisture feedback is quite different from RRTM scheme, suggesting that the moisture feedback prescribed in BOG radiation scheme is possibly too strong compared to the real climate state. Although the water vapor is only specified in radiation code, other processes associated with the advection and latent heat release are still retained in BOG radiation scheme, that is why the runs without moisture feedback (BOG-qctrl) behave so similarly to Frierson scheme. As illustrated in Figure 1.8, there is still slight amplified surface temperature change at high latitudes even if no

moisture feedback in radiation schemes, and therefore other mechanisms need to be investigated.

1.4.3 Heat transport

The total northward energy transport (TET) H across each latitude (ϕ) is calculated by the energy budget balance in an atmospheric column,

$$H(\varphi) = \int_{-\frac{\pi}{2}}^{\varphi} 2\pi a^2 (ASR - OLR) \cos \varphi \, \mathrm{d}\,\varphi, \qquad (1.10)$$

where ASR is the absorbed solar radiation flux and OLR is outward longwave radiation flux at latitude band φ, and hence $ASR - OLR$ is the net TOA radiation. The TET can be decomposed into energy transport by atmosphere and ocean. In our auaplanet experiments, Q-flux is added as the oceanic heat transport, which is the same in all experiments and thus has no effect to the temperature responses after changing abledos. Therefore, the northward oceanic energy transport H_o is

$$H_o(\varphi) = -2\pi a^2 \int_{-\frac{\pi}{2}}^{\varphi} \cos \varphi F_s \, \mathrm{d}\,\varphi, \qquad (1.11)$$

and atmospheric energy transport H_a is

$$H_a(\varphi) = 2\pi a^2 \int_{-\frac{\pi}{2}}^{\varphi} \cos \varphi (ASR - OLR + F_s) \, \mathrm{d}\,\varphi, \qquad (1.12)$$

where F_s represents the surface energy budget and is given by

$$Fs = SW + LW - SH - LH + \nabla \cdot \boldsymbol{Q}, \qquad (1.13)$$

in which SW and LW are the net shortwave and longwave radiation flux at surface, SH is the sensible heat flux, LH is the latent heat flux and $\boldsymbol{Q}$ is the Q-flux. The northward atmospheric energy transport (AET) can be decomposed in further into latent heat transport (H_{LH}), which is related to latent heat release, and dry static

energy transport (H_{dry}) associated with the motion of dry air, which are given by

$$H_{LH}(\varphi) = 2\pi a^2 \int_{-\frac{\pi}{2}}^{\varphi} \cos\varphi L_v (E - P) \, \mathrm{d}\varphi, \qquad (1.14)$$

and

$$H_{dry} = H_a - H_{LH}, \qquad (1.15)$$

where E and P denote evaporation and precipitation respectively, and L_v is the specific latent heat capacity. The meridional energy transports mentioned above in all experiments for BOG, Frierson and RRTM radiation schemes are shown in the Figure 1.15 and the changes of energy transport after changing albedos are displayed in Figure 1.16.
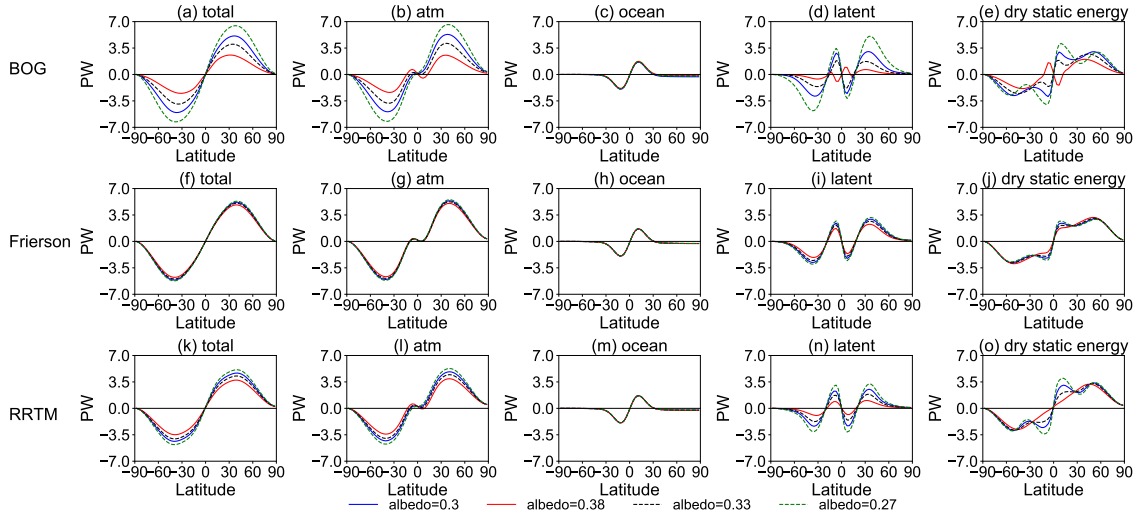

Figure 1.15 Heat transport in the experiments with different radiation schemes and various albedos. The top, middle and bottom panels are for the BOG, Frierson and RRTM radiation schemes respectively. Total northward heat transports are shown in (a), (f) and (k), the atmospheric heat transports are presented in (b), (g) and (l), the oceanic heat transport related to Q-flux are listed in (c), (h) and (m), the latent heat transport are illustrated in (d), (i) and (n), and the dry static energy transport are depicted in (e), (j) and (o). Blue solid, red solid, blue dash and green dash lines indicate the experiments where albedos are 0.3, 0.38, 0.33 and 0.27 respectively.

In the aquaplanet setups, the mixed layer is prescribed with same Q-flux symmetric to the equator in the experiments, and thus the northward ocean heat transports in all experiments resemble to each other (Figures 1.15c, h, m) and the differences when changing the albedos are nearly zero (Figures 1.16c, h, m). Therefore, the difference in total energy transport are from the atmospheric sources rather than

from oceanic ones. As for the response in atmospheric energy transport, the latent heat transport contributes a large portion. Previous studies have shown that an increase in atmospheric heat transport can cause midtropospheric warming in polar region [e.g., Screen et al., 2012], which can explain indirectly the polar amplification in experiments under seasonal or annual mean insolations [Kim et al., 2018]. Here we also examined the temperature change in polar region (70° northward) both at surface and mid-troposphere (450-700hPa) (Figure 1.17). The results show strong linear relationships between the total AET change across 70° and either the surface temperature change and ($R^2 = 0.98$, Figure 1.17a) or mid-troposphere temperature change ($R^2 = 0.93$, Figure 1.17b), implying that the heat transport is associated with the polar amplification both at surface and mid-troposphere under insolation conditions.
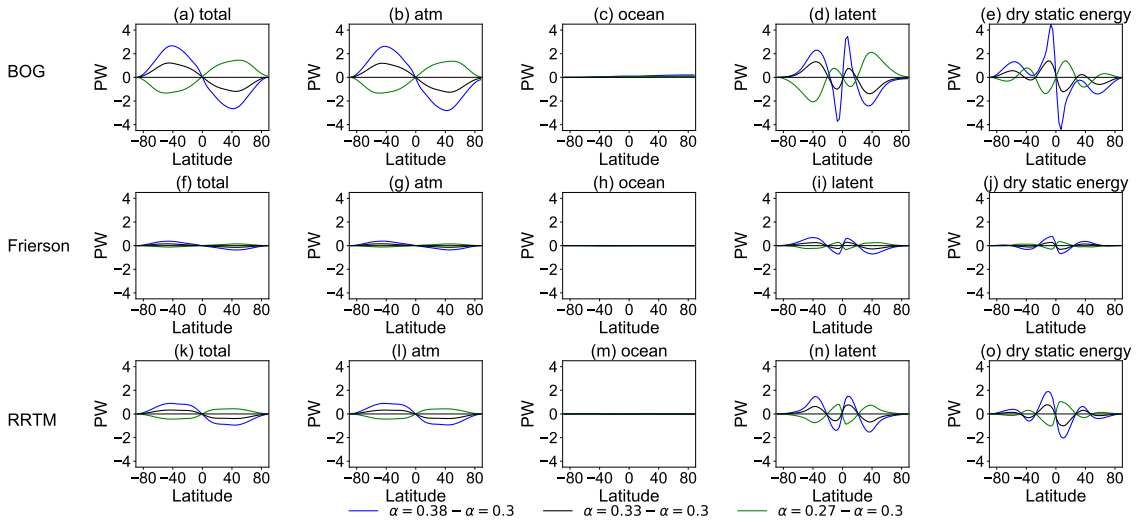

Figure 1.16 As in Figure 1.15, but for the difference in heat transport between in the experiments with different radiation schemes and various albedos. Blue, black and green solid lines indicates the difference between experiments where albedo is 0.38, 0.33 and 0.27 and the control experiment respectively.

1.4.4 Effect of climate feedbacks

In Section 1.3, with the aid of radiative kernel method, we have obtained the zonal mean radiative feedback parameters for BOG, Frierson and RRTM radiation schemes in Isca model (Figure 1.7), which enables us to investigate the relative importance of each feedback to zonal mean surface temperature change. Following Feldl and
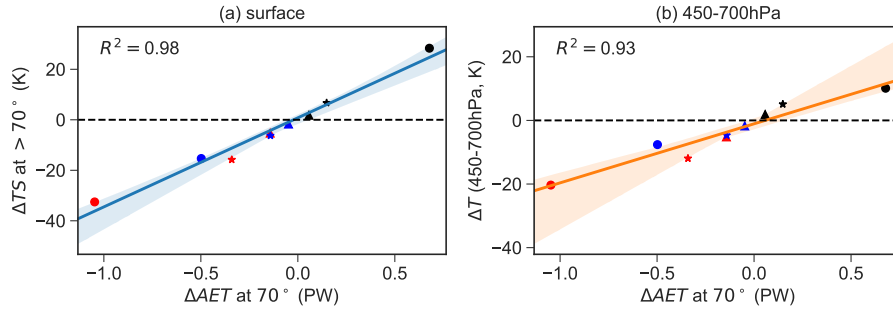
Figure 1.17 Changes of surface temperature poleward of 70° versus changes in atmospheric energy transport (AET) at 70° and the blue line is the linear regression of the two variables with the shading area indicating the 95% confidence interval. The solid circles, stars and triangles denote the BOG, Frierson and RRTM schemes respectively, and red, blue and black markers represent the runs in which the albedos are changed from 0.3 to 0.38, 0.33 and 0.27 respectively.

Roe [2013a] and Kim et al. [2018], we decompose the surface temperature change into various components after rearranging the Eq. (1.4):

$$\Delta T_s = \frac{1}{\overline{\lambda_P}}\left[\Delta R - \left(\lambda'_P + \sum_i \lambda_{NP_i}\right)\Delta T_s - \Delta\mathscr{F}\right],\qquad(1.16)$$

where $\overline{\lambda_P}$ designates the global mean Planck feedback, by which all the feedbacks will be normalized, including the local deviation of Planck feedback (λ'_P) from its global mean and all the other non-Planck feedbacks (λ_{NP_i}). As mentioned earlier, the cloud feedback and albedo feedback are not included in the experiments and thus lapse rate and water vapor feedback are the only two non-Planck feedbacks in Eq. (1.16). ΔR is the net TOA radiative flux and it should be equal to the change in the convergence of horizontal atmospheric heat flux, referred as the heat transport term. $\Delta\mathscr{F}$ is the forcing after changing albedos estimated by fixed-SST method.

The contributions to the zonal mean surface temperature change in BOG, Frierson and RRTM radiation schemes are displayed in Figure 1.18. We first look at the results from RRTM radiation scheme as it provides the relative realistic simulations. As shown in Figures 1.18g-i, the sum of different components (red thick dash-dotted line) reproduces the actual surface temperature change (blue thick solid line) in RRTM scheme either in cooling (Figures 1.18g, h) or warming (Figure 1.18i) cases, which implies we can analyze the relative importance of various components. As analyzed by Pithan and Mauritsen [2014], the Planck feedback itself will auto-

matically cause greater temperature change in high latitudes. In fact, according to Stefan-Boltzmann law, the longwave radiation emitted by earth surface (R_s) is

$$R_s = \epsilon \sigma T^4, \tag{1.17}$$

where ϵ is surface emissivity, which is close to 1, and σ the Stefan-Boltzmann constant with value of 5.67×10^{-8} Wm^{-2}K^{-1}. Assuming there is an uniform radiation disturbance (ΔR) at TOA, the surface temperature has to change by ΔT to balance ΔR, and ΔT given by

$$\Delta T = \frac{\Delta R_s}{4\epsilon \sigma T^3} = \frac{\Delta R}{4\epsilon \sigma T^3}, \tag{1.18}$$

in which ΔR_s is the radiation change at the surface. It is clear that the temperature response (ΔT) is large when the temperature (T) is low (e.g. polar region) and ΔT is small when T is relative high (e.g. tropical region). Therefore, the temperature response from Planck feedbacks (orange lines in Figures 1.18g-i) is large at high latitudes and small at low latitudes. It should be pointed out that the Planck feedback is a negative feedback, but here the Figure 1.18 shows the local deviation of Planck feedback from its global mean value and that's why the temperature response is negative in Figures 1.18g, h, and positive in Figure 1.18i. For the temperature response caused by lapse rate feedback (green solid lines in Figures 1.18g-i), it is positive in polar region and negative in tropical region in warming case and the signs are opposite in cooling case, indicating that the lapse rate feedback will amplify the temperature response in high latitudes. The positive lapse rate feedback in polar region is due to the bottom-heavy warming/cooling vertical structure (Figure 1.10). Our finding in warming case is consistent with result under equinox insolation in Kim et al. [2018], but things are different under seasonal and annual mean insolation conditions in which the lapse rate feedbacks are globally negative (Figure 1.19), which is because the temperature change is not enough to form an inversion layer near the surface [Kim et al., 2018].

The heat transport contributes most to the surface temperature change in polar
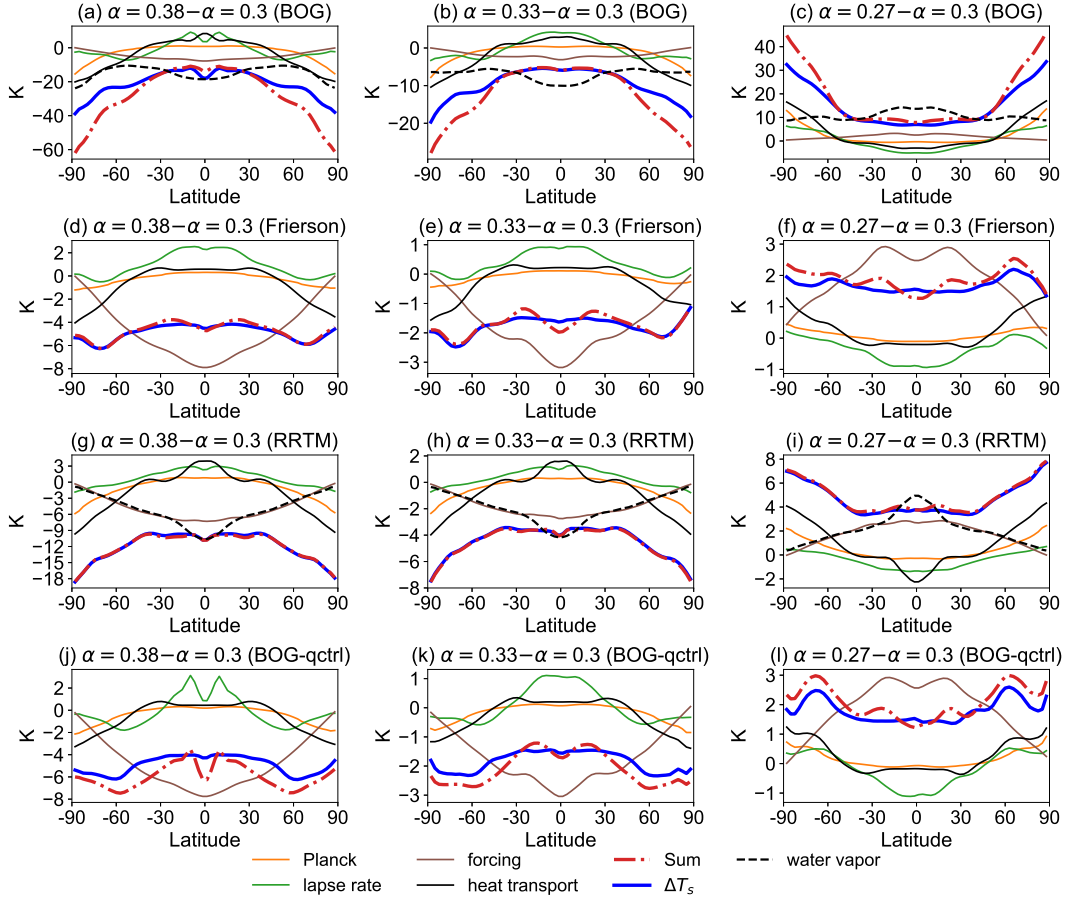
Figure 1.18 Zonal and annual mean contributions of surface temperature changes for (a)-(c) BOG scheme, (d)-(f) Frierson scheme, (g)-(i) RRTM schemes and (j)-(l) BOG scheme without moisture feedback respectively. The components include Planck feedback (orange), lapse rate feedback (green), forcing (brown), water vapor feedback (black dashed) and heat transport (black solid), all of which are weighted by global and annual mean of Planck feedback following Feldl and Roe [2013b] and Kim et al. [2018]. The sum of the different components is shown in thick red dash-dotted lines and the surface temperature change in experiments is indicated by thick blue lines. The first, second and third columns are for experiments when albedo is changed from 0.3 to 0.38, 0.33 and 0.27 respectively.
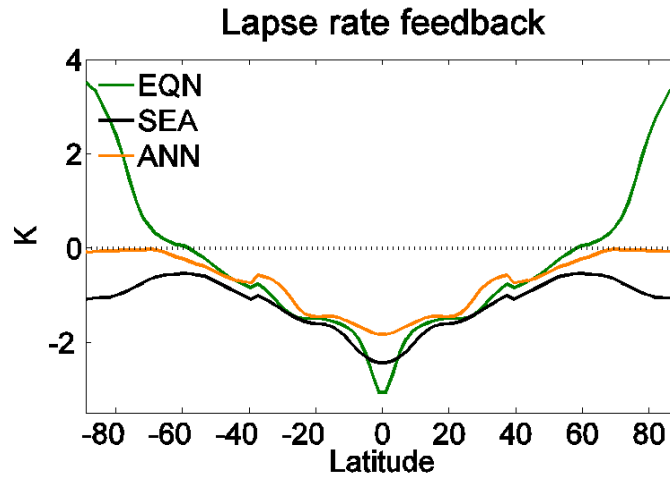

Figure 1.19 Zonal- and time-mean partial temperature changes (K) attributed to lapse rate feedback in GFDL AM2 under equinox (EQN, green), seasonal (SEA, black), and annual mean (ANN, orange) insolation. Adapted from Figure S1 of Kim et al. [2018].

region both in cooling and warming case in our study, but it is different from the calculation of Pithan and Mauritsen [2014], where they find that the temperature related feedbacks contribute most to the Arctic warming when there is a surface albedo feedback. When lack of surface albedo feedback, the heat transport is also the largest contributor to the polar amplification under seasonal solar radiation according to Kim et al. [2018]. In the warming case (Figure 1.18i), the heat transport cools the low latitudes and warms the high latitudes, which decreases the large meridional temperature and energy imbalance gradients. As illustrated in Figures 1.18g-i, the water vapor feedbacks contribute more to the tropical warming or cooling rather than to polar regions, which is consistent with the conclusion of Pithan and Mauritsen [2014]. But water vapor does have effect on the temperature change due to the enlarged climate sensitivity [Langen et al., 2012]. In fact, the temperature responses due to water vapor feedbacks in BOG scheme (black dashed lines in Figures 1.18a-c) are different from that in RRTM schemes, they don't tend to zero as latitudes increasing. Instead, they are relative flat at high latitudes, which could possibly be used to explain the abnormal surface temperature response in BOG scheme. Regarding the forcing (brown lines in Figures 1.18g-i) due to the change of albedos, it is larger in low latitudes than in high latitudes as the solar radiation is strong at low latitudes, and hence it will amplify the temperature change at low latitudes.

The roles of lapse rate feedback, Planck feedback and heat transport in BOG (Figures 1.18a-c) and Frierson (Figures 1.18d-f) schemes are similar to those in RRTM scheme, except the role of water vapor feedback in BOG scheme, which is much larger at high latitudes compared to others. One strange thing is the sum of these contributions is greater than the actual temperature response at high latitude in BOG scheme, for which a possible reason is that the decomposition of the surface temperature change is linear and some non-linear factors may have an influence at the high latitudes. We can see that after the water vapor feedback being disabled in BOG scheme, the sum of these various components is close to ΔT_s (Figures 1.18j-l), indicating that the non-linear effect is possible associated with water vapor.

1.5 Discussion and Summary

In this chapter, we employ the Isca model to study the zonal mean surface temperature change in aquaplanet simulation with various radiation schemes and albedos in order to quantify the different mechanisms that could lead to polar amplification of surface temperature change under equinox insolation. Two gray radiation schemes, BOG and Frierson, and one full radiation scheme, RRTM, are utilized in the simulations, where the BOG scheme shows the largest surface temperature change and polar amplification, while Frierson scheme show the weakest surface temperature change when changing albedos.

The comparison of results from BOG and Frierson gives us some insights about the role of water vapor feedback in surface temperature change. After turning off the water vapor feedback in the BOG scheme, the surface temperature responses are much smaller and become close to the simulation results from Frierson scheme. However, there is still the slight amplified surface temperature change at high latitudes, which is associated with the poleward atmospheric energy transport. Following Feldl and Roe [2013a] and Kim et al. [2018], the decomposition of the surface temperature change illustrate the relative importance of various contributions to surface temperature change at high latitudes. Specifically, heat transport, Planck feedback and the positive lapse rate feedback at polar region are all supportive to the polar amplification. However, water vapor feedback and the forcing induced by altering albedo contribute more to the surface temperature change at low latitudes than at high latitudes. In spite of that, the water vapor feedback is too strong at high latitudes in BOG scheme, which may explain the large temperature response in the experiments.

In sum, our findings have confirmed that polar amplification could exist even without sea ice and surface albedo feedback in aquaplanet simulations, which is consistent with the previous results [Alexeev et al., 2005; Kim et al., 2018; Langen and Alexeev, 2007]. However, we haven't explored the role of clouds to polar amplification due to lack of cloud schemes in Isca model currently. As assessed by Kim et al. [2018], the cloud radiative effects is negative in high latitudes due to an

increase of low-level cloud amount and positive in low latitudes due to a decrease of overall cloud amount, which could explain in part why the polar amplification of surface temperature is large in our simulations.

Bibliography

Alexeev, V. A., P. L. Langen, and J. R. Bates, 2005: Polar amplification of surface warming on an aquaplanet in "ghost forcing" experiments without sea ice feedbacks. *Climate Dynamics*, **24 (7-8)**, 655–666, doi:10.1007/s00382-005-0018-3.

Bony, S., and Coauthors, 2006: How well do we understand and evaluate climate change feedback processes? *Journal of Climate*, **19 (15)**, 3445–3482, doi:10.1175/ JCLI3819.1.

Byrne, M. P., and P. A. O'Gorman, 2013: Land-ocean warming contrast over a wide range of climates: Convective quasi-equilibrium theory and idealized simulations. *Journal of Climate*, **26 (12)**, 4000–4016, doi:10.1175/JCLI-D-12-00262.1.

Cai, M., 2005: Dynamical amplification of polar warming. *Geophysical Research Letters*, **32 (22)**, 1–5, doi:10.1029/2005GL024481.

Cai, M., 2006: Dynamical greenhouse-plus feedback and polar warming amplification. Part I: A dry radiative-transportive climate model. *Climate Dynamics*, **26 (7-8)**, 661–675, doi:10.1007/s00382-005-0104-6.

Ceppi, P., F. Brient, M. D. Zelinka, and D. L. Hartmann, 2017: Cloud feedback mechanisms and their representation in global climate models. *Wiley Interdisciplinary Reviews: Climate Change*, **8**, doi:10.1002/wcc.465.

Clough, S. A., M. W. Shephard, E. J. Mlawer, J. S. Delamere, M. J. Iacono, K. Cady-Pereira, S. Boukabara, and P. D. Brown, 2005: Atmospheric radiative transfer

modeling: A summary of the AER codes. *Journal of Quantitative Spectroscopy and Radiative Transfer*, **91 (2)**, 233–244, doi:10.1016/j.jqsrt.2004.05.058.

Feldl, N., B. T. Anderson, and S. Bordoni, 2017: Atmospheric eddies mediate lapse rate feedback and arctic amplification. *Journal of Climate*, **30 (22)**, 9213–9224, doi:10.1175/JCLI-D-16-0706.1.

Feldl, N., and S. Bordoni, 2016: Characterizing the Hadley circulation response through regional climate feedbacks. *Journal of Climate*, **29 (2)**, 613–622, doi: 10.1175/JCLI-D-15-0424.1.

Feldl, N., and G. H. Roe, 2013a: Four Perspectives on Climate Feedbacks. *Geophysical Research Letters*, **40 (15)**, 4007–4011, doi:10.1002/grl.50711.

Feldl, N., and G. H. Roe, 2013b: The nonlinear and nonlocal nature of climate feedbacks. *Journal of Climate*, **26 (21)**, 8289–8304, doi:10.1175/JCLI-D-12-00631.1.

Frierson, D. M. W., I. M. Held, and P. Zurita-Gotor, 2006: A Gray-Radiation Aquaplanet Moist GCM. Part I: Static Stability and Eddy Scale. *Journal of the Atmospheric Sciences*, **63 (10)**, 2548–2566, doi:10.1175/JAS3753.1.

Geen, R., A. Czaja, and J. D. Haigh, 2016: The effects of increasing humidity on heat transport by extratropical waves. *Geophysical Research Letters*, **43 (15)**, 8314–8321.

Goosse, H., and Coauthors, 2018: Quantifying climate feedbacks in polar regions. *Nature Communications*, **9 (1)**, doi:10.1038/s41467-018-04173-0.

Graversen, R. G., P. L. Langen, and T. Mauritsen, 2014: Polar amplification in CCSM4: Contributions from the lapse rate and surface albedo feedbacks. *Journal of Climate*, **27 (12)**, 4433–4450, doi:10.1175/JCLI-D-13-00551.1.

Graversen, R. G., and M. Wang, 2009: Polar amplification in a coupled climate model with locked albedo. *Climate Dynamics*, **33 (5)**, 629–643, doi: 10.1007/s00382-009-0535-6.

Gregory, J. M., 2004: A new method for diagnosing radiative forcing and climate sensitivity. *Geophysical Research Letters*, **31 (3)**, L03 205, doi:10.1029/ 2003GL018747.

Hall, A., 2004: The role of surface albedo feedback in climate. *Journal of Climate*, **17 (7)**, 1550–1568, doi:10.1175/1520-0442(2004)017⟨1550:TROSAF⟩2.0.CO;2.

Hansen, J., A. Lacis, D. Rind, G. Russell, P. Stone, I. Fung, R. Ruedy, and J. Lerner, 1984: Climate sensitivity: Analysis of feedback mechanisms. *Climate Processes and Climate Sensitivity, Geophysical Monograph*, **29**, 130–163, doi:10.1029/GM029p0130.

Hansen, J., M. Sato, and R. Ruedy, 1997: Radiative forcing and climate response. *Journal of Geophysical Research: Atmospheres*, **102 (D6)**, 6831–6864.

Hansen, J., and Coauthors, 2005: Efficacy of climate forcings. *Journal of Geophysical Research D: Atmospheres*, **110 (18)**, 1–45, doi:10.1029/2005JD005776.

Huang, Y., Y. Xia, and X. Tan, 2017: On the pattern of CO2 radiative forcing and poleward energy transport. *Journal of Geophysical Research: Atmospheres*, **122 (20)**, 10 578–10 593, doi:10.1002/2016JD025418.

IPCC, 2007: *Fourth Assessment Report: Climate Change 2007: The AR4 Synthesis Report.* Geneva: IPCC.

Johannessen, O. M., and Coauthors, 2004: Arctic climate change: Observed and modelled temperature and sea-ice variability. *Tellus, Series A: Dynamic Meteorology and Oceanography*, **56**, 328–341, doi:10.1111/j.1600-0870.2004.00060.x.

Kim, D., S. M. Kang, Y. Shin, and N. Feldl, 2018: Sensitivity of polar amplification to varying insolation conditions. *Journal of Climate*, **31 (12)**, 4933–4947, doi: 10.1175/JCLI-D-17-0627.1.

Langen, P. L., and V. A. Alexeev, 2007: Polar amplification as a preferred response in an idealized aquaplanet GCM. *Climate Dynamics*, **29 (2-3)**, 305–317, doi: 10.1007/s00382-006-0221-x.

Langen, P. L., R. G. Graversen, and T. Mauritsen, 2012: Separation of contributions from radiative feedbacks to polar amplification on an aquaplanet. *Journal of Climate*, **25 (8)**, 3010–3024, doi:10.1175/JCLI-D-11-00246.1.

Liu, R., H. Su, K. N. Liou, J. H. Jiang, Y. Gu, S. C. Liu, and C. J. Shiu, 2018: An Assessment of Tropospheric Water Vapor Feedback Using Radiative Kernels. *Journal of Geophysical Research: Atmospheres*, **123 (3)**, 1499–1509, doi:10.1002/2017JD027512.

Manabe, S., and R. T. Wetherald, 1975: The Effects of Doubling the CO2 Concentration on the climate of a General Circulation Model. *Journal of the Atmospheric Sciences*, **32 (1)**, 3–15.

Merlis, T. M., and M. Henry, 2018: Simple estimates of polar amplification in moist diffusive energy balance models. *submitted to Journal of Climate*, 1–13.

Park, K., S. M. Kang, D. Kim, M. F. Stuecker, and F.-F. Jin, 2018: Contrasting local and remote impacts of surface heating on polar warming and amplification. *Journal of Climate*, JCLI–D–17–0600.1, doi:10.1175/JCLI-D-17-0600.1.

Pendergrass, A. G., A. Conley, and F. M. Vitt, 2018: Surface and top-of-Atmosphere radiative feedback kernels for cesm-cam5. *Earth System Science Data*, **10 (1)**, 317–324, doi:10.5194/essd-10-317-2018.

Pithan, F., and T. Mauritsen, 2014: Arctic amplification dominated by temperature feedbacks in contemporary climate models. *Nature Geoscience*, **7 (3)**, 181–184, doi:10.1038/ngeo2071.

Polyakov, I. V., and Coauthors, 2002: Observationally based assessment of polar amplification of global warming. *Geophysical Research Letters*, **29 (18)**, 25–1–25–4, doi:10.1029/2001GL011111.

Schneider, E. K., B. P. Kirtman, and R. S. Lindzen, 1999: Tropospheric Water Vapor and Climate Sensitivity. *Journal of the Atmospheric Sciences*, **56**, 1649–1658, doi:10.1175/1520-0469(1999)056⟨1649:TWVACS⟩2.0.CO;2.

Screen, J. A., C. Deser, and I. Simmonds, 2012: Local and remote controls on observed Arctic warming. *Geophysical Research Letters*, **39 (10)**, L10 709, doi: 10.1029/2012GL051598.

Screen, J. A., and I. Simmonds, 2010: The central role of diminishing sea ice in recent Arctic temperature amplification. *Nature*, **464 (7293)**, 1334–1337, doi: 10.1038/nature09051.

Serreze, M. C., and R. G. Barry, 2011: Processes and impacts of Arctic amplification: A research synthesis. *Global and Planetary Change*, **77 (1-2)**, 85–96, doi:10.1016/ j.gloplacha.2011.03.004.

Serreze, M. C., and J. A. Francis, 2006: The arctic amplification debate. *Climatic Change*, **76 (3-4)**, 241–264, doi:10.1007/s10584-005-9017-y.

Shell, K. M., J. T. Kiehl, and C. A. Shields, 2008: Using the radiative kernel technique to calculate climate feedbacks in NCAR's Community Atmospheric Model. *Journal of Climate*, **21 (10)**, 2269–2282, doi:10.1175/2007JCLI2044.1.

Soden, B. J., and I. M. Held, 2006: An Assessment of Climate Feedbacks in Coupled Ocean Atmosphere Models. *Journal of Climate*, **19 (2003)**, 3354–3360, doi: 10.1175/JCLI9028.1.

Soden, B. J., I. M. Held, R. C. Colman, K. M. Shell, J. T. Kiehl, and C. A. Shields, 2008: Quantifying climate feedbacks using radiative kernels. *Journal of Climate*, **21 (14)**, 3504–3520, doi:10.1175/2007JCLI2110.1.

Taylor, P. C., M. Cai, A. Hu, J. Meehl, W. Washington, and G. J. Zhang, 2013: A decomposition of feedback contributions to polar warming amplification. *Journal of Climate*, **26 (18)**, 7023–7043, doi:10.1175/JCLI-D-12-00696.1.

Vallis, G. K., and Coauthors, 2018: Isca, v1.0: A framework for the global modelling of the atmospheres of Earth and other planets at varying levels of complexity. *Geoscientific Model Development*, **11 (3)**, 843–859, doi:10.5194/gmd-11-843-2018.

Vavrus, S., 2004: The impact of cloud feedbacks on Arctic climate under Greenhouse forcing. *Journal of Climate*, **17 (3)**, 603–615, doi:10.1175/1520-0442(2004) 017⟨0603:TIOCFO⟩2.0.CO;2.

Wetherald, R. T., and S. Manabe, 1988: Cloud Feedback Processes in a General Circulation Model. *Journal of the Atmospheric Sciences*, **45 (8)**, 1397–1416, doi: 10.1175/1520-0469(1988)045⟨1397:CFPIAG⟩2.0.CO;2.

Winton, M., 2006: Amplified Arctic climate change: What does surface albedo feedback have to do with it? *Geophysical Research Letters*, **33 (3)**, 1–4, doi: 10.1029/2005GL025244.